

The Fourcade-Figueroa galaxy: a clearly disrupted superthin edge-on galaxy[★]

J. Saponara^{1,2}, P. Kamphuis³, B. S. Koribalski^{4,5}, and P. Benaglia¹

¹ Instituto Argentino de Radioastronomía, CONICET-CICPBA-UNLP, CC5 (1897) Villa Elisa, Prov. de Buenos Aires, Argentina
e-mail: jsaponara@iar-conicet.gov.ar

² Facultad de Ciencias Astronómicas y Geofísicas, UNLP, Paseo del Bosque s/n, 1900, La Plata, Argentina

³ Ruhr University Bochum, Faculty of Physics and Astronomy, Astronomical Institute, 44780 Bochum, Germany

⁴ CSIRO Astronomy and Space Science, Australia Telescope National Facility, P.O. Box 76, Epping, NSW 1710, Australia

⁵ Western Sydney University, Locked Bag 1797, Penrith, NSW 2751, Australia

June 10, 2021

ABSTRACT

Context. Studies of the stellar and the H I gas kinematics in dwarf and Low Surface Brightness (LSB) galaxies are essential for deriving constraints on their dark matter distribution. Moreover, a key component to unveil in the evolution of LSBs is why some of them can be classified as superthin.

Aims. We aim to investigate the nature of the proto-typical superthin galaxy Fourcade-Figueroa (FF), to understand the role played by the dark matter halo in forming its superthin shape and to investigate the mechanism that explains the observed disruption in the approaching side of the galaxy.

Methods. Combining new H I 21-cm observations obtained with the Giant Metrewave Radio Telescope with archival data from the Australia Telescope Compact Array we were able to obtain sensitive H I observations of the FF galaxy. These data were modelled with a 3D tilted ring model in order to derive the rotation curve and surface brightness density of the neutral hydrogen. We subsequently used this model, combined with a stellar profile from the literature, to derive the radial distribution of the dark matter in the FF galaxy. Additionally, we used a more direct measurement of the vertical H I gas distribution as a function of the galactocentric radius to determine the flaring of the gas disk.

Results. For the FF galaxy the Navarro-Frenk-White dark matter distribution provides the best fit to the observed rotation curve. However, the differences with a pseudo-isothermal halo are small. Both models indicate that the core of the dark matter halo is compact. Even though the FF galaxy classifies as superthin, the gas thickness about the galactic centre exhibits a steep flaring of the gas which is in agreement with the edge of the stellar disk. Besides, FF is clearly disrupted towards its north-west-side, clearly observed at both, optical and H I wavelengths. As suggested previously in the literature, the compact dark matter halo might be the main responsible for the superthin structure of the stellar disk in FF. This idea is strengthened through the detection of the mentioned disruption; the fact that the galaxy is disturbed also seems to support the idea that it is not isolation that cause its superthin structure.

Conclusions.

Key words. galaxies: groups: individual: ESO 270–G017 — galaxies: interactions — radio lines: galaxies

1. Introduction

In 1993, Karachentsev, Karachentseva and Parnovskij published the Flat Galaxy Catalogue (FGC, Karachentsev et al. 1993), and a revised version of it in 1999 (RFGC, Karachentsev et al. 1999). The catalogue contains disk-like edge-on galaxies with a major-to-minor stellar axis ratio $a/b > 7$. Superthin galaxies are a special kind of flat galaxies with $a/b \gtrsim 10$. These are gas-rich Low Surface Brightness (LSB) galaxies, with little or no obvious bulge component, minimal dust absorption (Matthews & Wood 2001), blue optical colours (Dalcanton & Bernstein 2000), low metallicities (Roennback & Bergvall 1995), low current star formation and a high ratio of dynamic to H I mass (de Blok & Bosma 2002). These characteristics suggest that such galaxies are some of the least evolved galaxies in the Universe. Besides, their high-inclinations and simple structure allow us to

study the influences produced by internal as well as external processes (Uson & Matthews 2003). All the mentioned characteristics set the superthin galaxies as ideal laboratories to investigate the early stages of disk galaxy evolution.

The cosmological paradigm of hierarchical galaxy formation and evolution proposes that galaxies are subject to merging and interaction. Thus, the disk structure and thickness in galaxies are affected by the environment (Toth & Ostriker 1992; Odewahn 1994; Reshetnikov & Combes 1997; Schwarzkopf & Dettmar 2001). This suggests that a flat disk galaxy must remain isolated to persist as a superthin. However, some of these galaxies are found in groups of galaxies as well as in the field (Kautsch 2009). Therefore, the question arises on how does the pure disk survive? A possible explanation is the presence of a massive dark matter (DM) halo which stabilises their disks against perturbations (Zasov et al. 1991; Gerritsen & de Blok 1999); moreover, Mosenkov et al. (2010) found a correlation between the thickness of stellar disks and relative mass of the dark matter halo. Banerjee & Jog (2013) showed that the determination of the superthin disk distribution, in low-luminosity bulge-less

[★] The reduced ATCA+GMRT data cube as a FITS file is only available at the CDS via anonymous ftp to cdsarc.u-strasbg.fr (130.79.128.5) or via <http://cdsweb.u-strasbg.fr/cgi-bin/qcat?J/A+A/>

galaxies, is ruled by the compactness of the DM. This idea is supported by the studies performed over the four superthin and proto-typical superthin galaxies UGC 7321 (O’Brien et al. 2010; Banerjee & Bapat 2017), IC 2233, IC 5249 (Banerjee & Bapat 2017) and FGC 1540 (Kurapati et al. 2018). As this sample is still extremely small any single addition to it can still provide significant new insights or strengthen the current ideas about the nature of superthin galaxies.

Studies of the stellar and the H I gas kinematics in dwarf and LSB galaxies are essential for deriving constraints on the DM distribution (Rubin et al. 1978; McGaugh & de Blok 1998; Banerjee et al. 2010). Moreover, understanding why some LSBs are superthin can contribute to the overall understanding of LSBs and DM in general. In this paper we focus on the prototypical superthin Fourcade-Figueroa (FF) galaxy. By combining new Giant Metrewave Radio Telescope (GMRT) data with archival Australia Telescope Compact Array (ATCA) data we obtained a high resolution sensitive H I observation of the galaxy. After modelling the gas distribution we use the derived rotation curve to determine the DM distribution in the FF galaxy.

The FF galaxy, also known as ESO 270–G017, was discovered in 1970 (Fourcade 1970) as an elongated and diffuse object, see Fig. 1, located approximately at $2^{\circ} 32'$ southeast of the core of the radio galaxy Centaurus A (Cen A; NGC 5128). The galaxy was initially thought to be part of the Centaurus A group (Colomb et al. 1984; Tully et al. 2013; Karachentsev & Kudrya 2014). However, recent distance estimates place it just beyond Centaurus A at a distance of 7 Mpc (Karachentsev et al. 2015). The ratio b/a is a strong parameter to determine the flatness of a galaxy, since typical b/a measurements of flat galaxies (between 0.04 to 0.14, Karachentsev et al. 1999) are quite different from the usual values found in the literature regarding all types. The major and minor axes can also be used to derive the galaxy inclination i on a first approximation, as $\cos(i) = b/a$.

We listed the main optical properties of the FF galaxy in Table 1. From WISE observations Wang et al. (2017) obtained the two-dimensional structural surface brightness decomposition of FF. This profile has a scale length of 4.4 kpc. From their cleaned $3.4\ \mu\text{m}$ WISE image we determine an inner ($r < 2.8$ kpc) scale height of 0.47 kpc. This results in a ratio $h_r/h_z \sim 9.4$ confirming again that the FF galaxy can be considered a superthin galaxy (see also Kregel et al. 2002). FF is a good candidate to perform the mass-modelling and, thereby, determine its dark matter halo. Despite its superthin structure, the FF galaxy shows an asymmetry towards its northwest side (Fourcade 1970), like a shred or disruption, observed in both optical and H I images. The origin of this disruption remains unclear.

The paper is organised as follows: in Sect. 2 we describe the observations and data reduction, including the combination process between data sets from very different radio interferometers; in Sec. 3 we present the H I distribution and kinematics; in Sect. 4 we describe the mass models; in Sec. 5 we present the mass-modelling results and the discussion; in Sec. 6 the shred and in Sect. 7 the summary.

2. HI Observations and data reduction

The FF galaxy has been observed at 1420 MHz with the Australia Telescope Compact Array (ATCA). The data were downloaded from the Australia Telescope Online Archive (ATOA¹). The data were published by Koribalski et al. (2018) and are part

¹ <https://atoa.atnf.csiro.au/>

Table 1. Optical properties of the Fourcade-Figueroa galaxy.

Properties		Ref.
Morphology type	SB(s)m	(1)
α (J2000) [h m s]	13:34:47.3	
δ (J2000) [$^{\circ}$ ' '']	−45:32:51	
D [Mpc]	6.95	(2)
m_B	11.7	(3)
D_{B25} [']	11.3	(3)
A_B	0.48	(4)
M_B [mag]	−18	
L_B [$L_{\odot,B}$]	2.4×10^9	
$F_{H\alpha}$ [$\text{erg cm}^{-2} \text{s}^{-1}$]	$(2.09 \pm 0.37) \times 10^{-12}$	(5)
$\log(SFR)$ [$M_{\odot} \text{yr}^{-1}$]	−1.0	
i [deg]	83	(4)
a/b	9.1	(6)

Ref.: references; (1) de Vaucouleurs et al. (1991), (2) Karachentsev et al. (2015), (3) ESO LV Lauberts & Valentijn (1989), (4) Schlegel et al. (1998), (5) Kennicutt et al. (2008), (6) Karachentsev et al. (1999).

of the Local Volume H I Survey (LVHIS) project. Notwithstanding the existence of previous observations, new ones were carried out at the same frequency with the GMRT, that provides better angular and velocity resolution. Additionally, it has better coverage of the uv -plane which can be further improved upon by using observations from both telescopes. In the following subsections we describe the observations and data calibration for both ATCA and GMRT as well as the combination process.

2.1. Australia Telescope Compact Array data

The ATCA 21-cm observations were carried out in January 1993, June and July 1993 as well as November 2008 using the 750, 6A and EW367 array configurations respectively. The total integration time on-source was 27 h 40 min. The 8 MHz bandwidth divided into 512 channels resulted in a spectral resolution of 15.6 kHz, equivalent to $\sim 4 \text{ km s}^{-1}$ per channel. A flux calibrator was observed at the beginning and the end of each observing run for 10 min while a phase calibrator was observed between the target scans every 45 min; see Table 2 for more details.

Data reduction and analysis were performed with the MIRIAD software (Sault et al. 1995) using standard procedures. We calibrated each data set separately, using PKS 0407–658 (750/6A array) and PKS 1934–638 (EW367 array) as primary flux and bandpass calibrators. PKS 1320–446 (750/6A array) and PKS 1421–490 (EW367 array) served as the phase calibrators. We used the MIRIAD task UVLIN to subtract the continuum. With a bandwidth of 8 MHz (see Table 2), we were able to select the line-free channels on either side of the detected H I emission.

2.2. Giant Metrewave Radio Telescope data

We observed the FF galaxy with the GMRT at 21-cm for a total time of ~ 14 h (project 28_069, PI P. Benaglia). The observations were carried out during June–July 2015 and January 2016 in the spectral zoom mode with the GMRT-Software backend. We used a 4.16 MHz bandwidth with 512 channels which results in a spectral resolution of 8.13 kHz, equivalent to 1.7 km s^{-1} per channel. The flux calibrator 3C 286 was observed at the beginning and the end of the run. The source 1323–448 was used as



Fig. 1. FF three-colour image composites from the B, V, and I bands published by Ho et al. (2011).

Table 2. ATCA and GMRT observing parameters.

	ATCA configuration			GMRT
	750A	6A	EW367	
Project	C245	C245	C1341	28_069
Date(s)	28-01-93/29-01-93	28-06-93/16-07-93	15-11-08	29-06, 04-07-15/ 07-07-15/26-01-16
Time on source [min]	474.9	588/544	597.0	195/501/196
Centre frequency [MHz]	1417	1417	1417	1414
Bandwidth [MHz]	8	8	8	4.16
Number of channels	512	512	512	512
Channel width [km s ⁻¹]	3.3	3.3	3.3	1.8
Velocity resolution [km s ⁻¹]	4	4	4	1.8
Primary beam [']		33		26.6

the phase calibrator and was observed between the target scans; see Table 2 for more details.

The data were flagged and calibrated using the FLAGCAL pipeline (Prasad & Chengalur 2011). Besides, we extensively used for further analysis, visualisation and multi-wavelength imaging the MIRIAD software package and kvis, part of the karma package (Gooch 1996). To check the calibration process, all the calibrator sources were imaged. GMRT does not do online Doppler tracking. Thus, the Astronomical Imaging Processing System (AIPS, Greisen 2003) task CVEL was implemented to apply the Doppler shift corrections. All the data sets were combined using the AIPS task DBCON. The continuum subtraction was made with MIRIAD task UVLIN; we were able to select the line-free channels on either side of the detected H I emission.

2.3. Combining ATCA and GMRT radio interferometer data

The benefits of complementing the GMRT with ATCA data are the improvement of the signal-to-noise ratio by ~15%, a better *uv* plane coverage that should improve the quality of the final images, and a better angular resolution. In this manner, we will get the most out of observations; we can map the extended structures with excellent angular resolution.

As the GMRT is a non-coplanar array we in principle should account for this when imaging the data, i.e a *w*-projection is required. However, for our current observations we estimate the shift introduced by ignoring this effect would lead to a shift of 2.25" at the first null of the primary beam over a 12h observation. This leads to a 10% error on the synthesised beam if we limit our baselines to be < 28 kλ. As MIRIAD is the only package that allows us to combine the data in the *uv*-domain while taking into account the primary beam correction we choose to

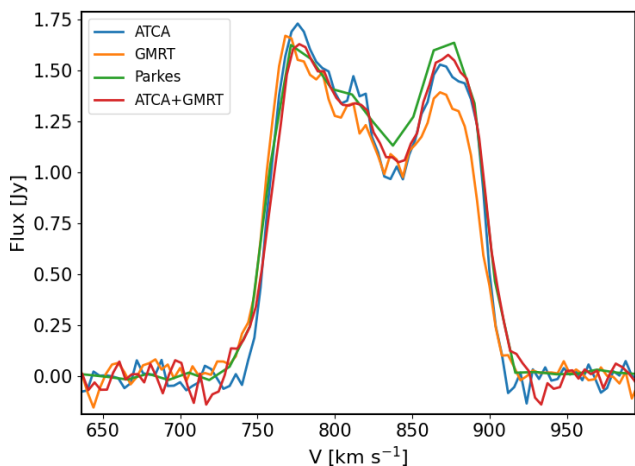


Fig. 2. Comparison of the FF global H I profile obtained using ATCA (light blue), GMRT (orange), Parkes (green, Koribalski et al. 2004) and the combination of ATCA and GMRT data (red).

image the data without a w -projection. As for both observation the band width was too narrow to perform a self-calibration, we conclude that this problem will not affect the image cubes if we just use the visibilities up to $28\text{ k}\lambda$ (equivalent to 6 km).

We carried out the data combination in the uv domain using the `MIRIAD` software. Both data sets need to have the same velocity system reference and channel increment organised in the same way; the tasks `CVEL`, `SPLIT` and `BLOAT` from `AIPS` were used to arrange the visibilities of the different observations on the same frequency grid. We implemented the `MIRIAD` routine `INVERT` to perform a linear mosaic of these 21-cm GMRT and ATCA data. The `INVERT` task optimises the signal-to-noise ratio using the system temperature. For such, once loaded the GMRT data sets into `MIRIAD` we had to add the value of the system temperature in the header. This parameter was gathered from the GMRT user’s manual². The deconvolution process was carried out using the Maximum Entropy deconvolution, `MOSMEM` task, for a mosaiced image. The final synthesised beam was created with task `MOSSPSF` and applied during restoration.

To summarise, the final H I cube was made using baselines up to $28\text{ k}\lambda$ and natural weighting. The synthesised beam is $20'' \times 20''$, which results in a physical resolution of $673\text{ pc} \times 673\text{ pc}$ at the adopted FF distance. The corresponding r.m.s. noise is 2 mJy beam^{-1} .

3. HI distribution and kinematics

To ensure that our combined data set is free from systematic biases we first extract the line spectrum and compared it to the individual datasets and an archival single dish observation. The results are shown in Fig. 2. The total line flux obtained from the combination data cube is $F_{\text{HI}} = 197 \pm 0.4\text{ Jy km s}^{-1}$, which is in agreement with the value present in the H I Parkes All-Sky Survey (HIPASS), $F_{\text{HI}} = 199.4 \pm 15.1\text{ Jy km s}^{-1}$ (Koribalski et al. 2004), and LVHIS (Koribalski et al. 2018) with the LVHIS $F_{\text{HI}} = 224.7\text{ Jy km s}^{-1}$.

The global H I profile of the FF galaxy is shown in Fig. 2. It can be appreciated that in the case of the profile derived from the combined cube (ATCA+GMRT data), the flux along the velocity axis remains, mostly, equal or below that derived from Parkes data alone, as it is expected.

The H I diameter is $D_{\text{HI}} = 20'$. The H I emission was detected from ~ 720 to 920 km s^{-1} . At a distance of 6.95 Mpc , this corresponds to a total H I mass of $M_{\text{HI}} = 2.2 \times 10^9\text{ M}_{\odot}$, which means that $M_{\text{HI}}/L_{\text{B}} = 1.04$. The systemic velocity of FF is 828 km s^{-1} . The profile widths of 20% and 50% levels are 142 km s^{-1} and 120 km s^{-1} .

3.1. H I distribution

Fig. 3 shows the channels where the FF galaxy contains detectable H I emission. A visible disruption is observed in the channels covering the velocity ranges from 770 to 810 km s^{-1} . The shred (Fourcade 1970; Thomson 1992) is clearly seen as a disruption in the distribution as well as the kinematics of the gas, and corresponds to the shred as seen in the optical. The disruption is at a projected radial distance $\sim 5\text{ kpc}$ from the centre, same position where the H I distribution bends away from the major axis to the north, see Fig. 4. The H I is distributed over a diameter of $\sim 20'$, almost two times the optical diameter ($\sim 11.3'$), see Fig. 4 top panels. The velocity field of FF is not regular as can be seen in Fig. 4 bottom left panel. The velocity dispersion varies between 5 and 15 km s^{-1} , see Fig. 4 bottom right panel. Note that since we are looking at a (nearly) edge-on galaxy, the measured dispersion indicates the spread in coherent rotation along any line of sight, rather than a physical gas velocity dispersion.

3.2. The vertical gas thickness

Considering the H I gas distribution in FF is asymmetric, we derive the thickness of the H I disk as a function of the galactocentric radius. The method we implemented follows the procedures laid out in Olling (1995) and O’Brien et al. (2010). The vertical H I profile of FF exhibits a high degree of asymmetry of the gas thickness about the galactic centre. In the receding side of the galaxy, the H I flares from a Full Width Half Max (FWHM) of 2.5 kpc at 5 kpc out to 3.5 kpc at 18 kpc . The steep flaring of the gas is in agreement with the edge of the stellar disk. Between 5 kpc and 15 kpc , the H I thickness seems to remain constant, except for a bump at 8 kpc . On the approaching side, the vertical H I thickness shows an irregular flaring profile. From 3 kpc to 5 kpc the H I thickness is roughly constant with an FWHM around 2 kpc . In the range between 5 kpc to 10 kpc , the H I gas flare from 2.3 kpc to 3.6 kpc which is in agreement with the location of the shred. The steep gas flare at the mentioned galactocentric distance is coincident with the radius where the stellar disk becomes fainter. Additionally, the line width of the velocity profiles (see Fig. 4) highly increases at this position. After 10 kpc (galactocentric radius), the H I disk thickness decreases at radii outside of 15 kpc ; this is in agreement with the decrease of the H I velocity dispersion. The linear size of the beam is $\sim 700\text{ pc}$, and Fig. 5 shows that variations on vertical gas thickness occur on a much larger scale (a few kpc, thus including several beams), then overriding –or at least minimising– beam smearing problems. On average z_0 is $32.6'' \pm 0.2''$ or $z_0 = 1.1 \pm 0.4\text{ kpc}$ at the assumed distance of 6.95 Mpc .

3.3. H I kinematics, 3D modelling and the rotation curve using FAT & TiRiFiC

The rotation curve was derived using the Fully Automatic TiRiFiC code (FAT, Kamphuis et al. 2015), which is a wrap-

² <http://gmrt.ncra.tifr.res.in>

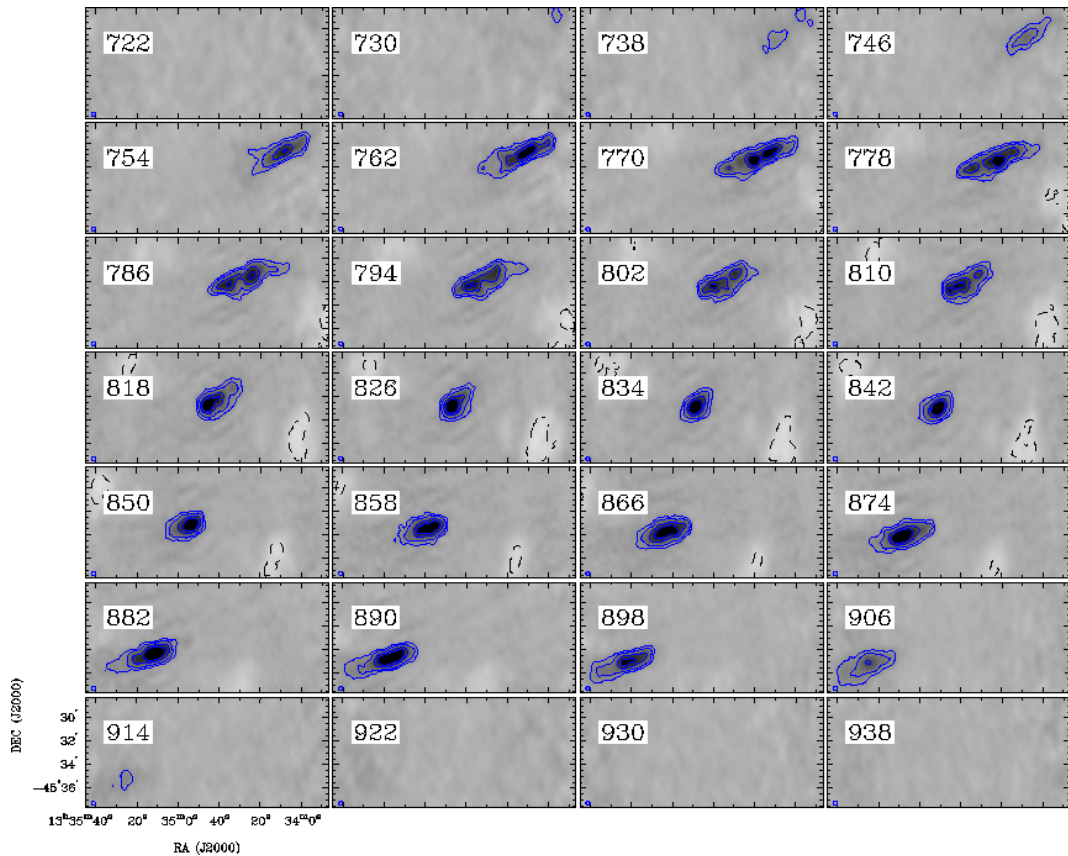


Fig. 3. ATCA+GMRT high-resolution H I channel maps of the Fourcade-Figueroa galaxy. The channel velocity is shown in the top left corner (in km s^{-1}) and the synthesised beam ($20''$) in the bottom left corner of each panel. The contour levels are $-6, 6, 15, 25, 35 \text{ mJy beam}^{-1}$.

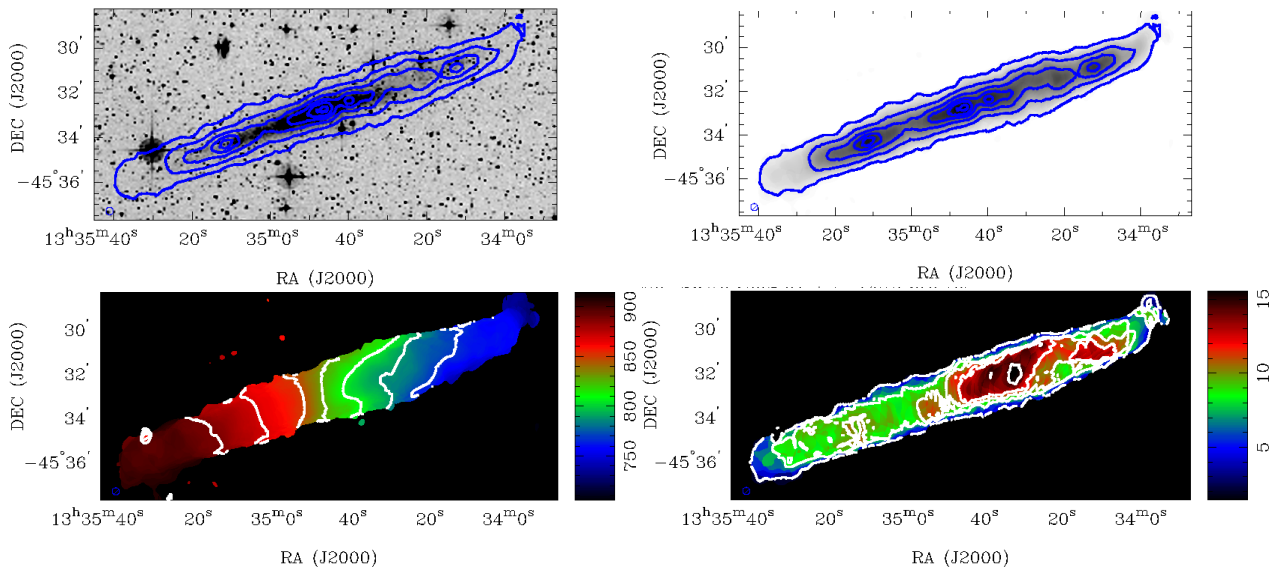


Fig. 4. ATCA+GMRT H I moment maps of the Fourcade-Figueroa galaxy. **Top left panel:** H I distribution overlaid on the DSS2 I -band image. The H I contour levels are $0.24, 0.9, 1.7, 2.1 \text{ Jy beam}^{-1} \text{ km s}^{-1}$. **Top right panel:** H I distribution (same contours). **Bottom left panel:** velocity field, the contour levels are $768, 788, 808, 828, 848, 868, 888 \text{ km s}^{-1}$. **Bottom right panel:** velocity dispersion; the contour levels are $3, 8, 10, 12, 15 \text{ km s}^{-1}$. The H I distribution maps were made using the low-resolution cube with a synthesised beam of $20'' \times 20''$.

per code around the Tilted Ring Fitting Code (TiRiFiC, Józsa et al. 2012), to perform a 3D modelling, and the Source Finder Application (SoFiA, Serra et al. 2015) to estimate the initial parameters. As it turns out FAT is not capable of dealing with the varying noise statistics, due to the primary beam correction. The final FAT model did not cover the full extent of the H I disk.

Therefore the outer parts of the galaxy were fitted manually with TiRiFiC itself. Performing a 3D modelling, by fitting the 3D observations directly as TiRiFiC and FAT routines do, guarantees that problems such as beam smearing and projection effects are overcome, according to Józsa et al. (2012) and Kamphuis et al. (2015). Since the FF galaxy is clearly warped and asymmetric,

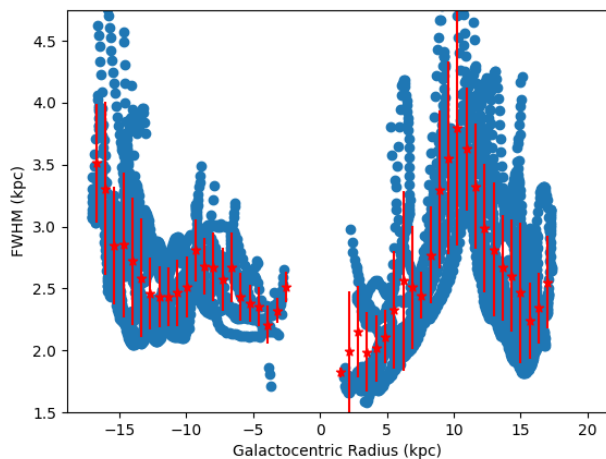


Fig. 5. Measured HI FWHM thickness (negative radius is receding).

we created a 2-disk model where each disk represents one half of the galaxy. The inclination was the most problematic parameter to fit; we attempt values between 80 and 90 degrees and after the visual inspection of the results we decided to fix it at 87 deg. From the vertical HI distribution analysis we obtained that on average z_0 is 1.1 ± 0.4 kpc; therefore, we decided to fix this value in the model as well. To check the validity of the fits, visual comparisons between the data and models were performed in many different representations of the cubes, such as channel map by channel map, the velocity field and the position velocity (pv) diagram parallel to the minor and major axis. For the error bars on the final rotation curve, we used the difference between the approaching and receding side; a minimum realistic error of 2 km s^{-1} was considered. Figure 6 shows that the rotation curve rises steeply in the innermost 4 kpc, then continues to rise slowly until the outermost radius. The maximum rotation speed is $\sim 72 \text{ km s}^{-1}$. The de-projected HI radial surface brightness profile derived by FAT shows the HI surface density peak at $\Sigma_{\text{HI}} \sim 5 \text{ M}_{\odot} \text{ pc}^{-2}$ in the centre but is mostly constant around $\sim 5 \text{ M}_{\odot} \text{ pc}^{-2}$ (see Fig. 6). The pv -diagram is shown in Fig. 7.

4. Mass models

4.1. Visible matter contribution

The rotation velocities due to the gravitational potentials of the stellar and gaseous disks were determined separately using the task ROTMOD of the Groningen Image Processing System (GIPSY, van der Hulst et al. 1992a). Since the old stellar population dominates the total stellar mass in late-type galaxies and mid-infrared emission is less susceptible to dust extinction and is also not affected by recent star formation, the stellar contribution (V_*) was derived using the stellar mass profile obtained by Wang et al. (2017) from WISE $3.4 \mu\text{m}$ infrared images. We assumed the vertical distribution as

$$D_*(z) = \frac{\exp(-\frac{|z|}{z_0})}{z_0},$$

where z_0 is the disk scale-height ($z_0=0.47$ kpc), see for instance van der Kruit & Searle (1981a,b). The gaseous contribution (V_{gas}) was derived using the de-projected HI radial surface density profile as derived by FAT and TiRiFiC. We considered a

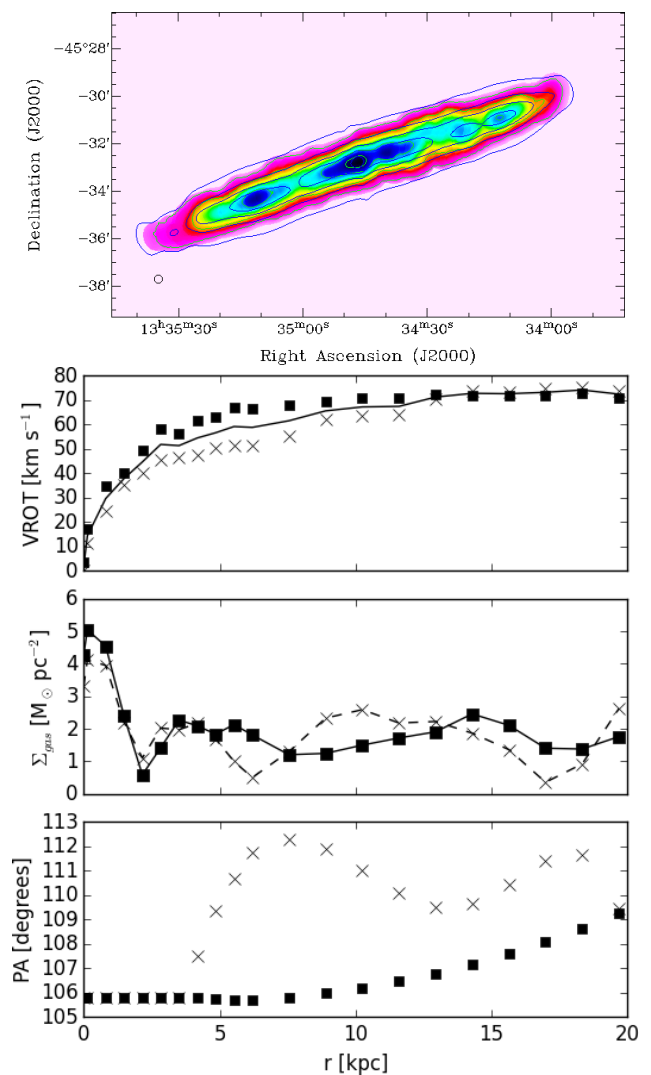


Fig. 6. **First row:** Comparison between data (green) and model (blue) moment zero maps. **From 2nd to 4th rows:** Model parameters as a function of radius. The crosses/squares represent the approaching/receding halves of the FF galaxy. **Second row:** Rotation curve, the solid curve corresponds to the mean rotation curve. **Third row:** The de-projected HI gas surface distribution. **Fourth row:** The position angle variation.

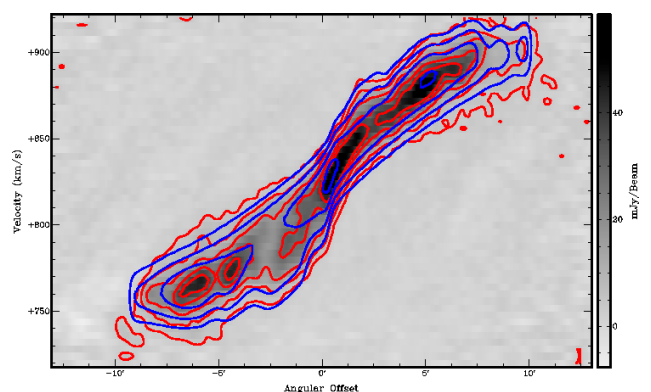


Fig. 7. The HI position-velocity (pv) diagram along the major axis is shown in grey colours and red contours while the blue contour levels represent the pv of the model galaxy; the contour levels are 4, 9, 17, 29, 39 $\text{mJy beam}^{-1} \text{ km s}^{-1}$.

vertical density distribution given by the exponential law

$$D_{\text{gas}}(z) = \frac{-\exp\left(\frac{z}{z_0}\right)}{z_0},$$

where the value of $z_0=1.1\pm 0.4$ kpc (see Sec. 3.2). The H I gas surface density distribution was then multiplied by a factor of 1.4 to account for the primordial helium, but we did not consider the presence of molecular H₂ in our models; for late-type LSB spiral galaxies the ratio H₂/HI is 10⁻³ (Matthews et al. 2005).

4.2. Dark Matter Halo

We used the so-called pseudo-isothermal halo (ISO) and the Navarro, Frenk & White (NFW) density profiles to model the DM halo of the FF galaxy.

- The simplest model for a DM halo density profile is the pseudo-isothermal halo (Begeman et al. 1991). Its density profile is given by

$$\rho_{\text{ISO}}(R) = \frac{\rho_0}{1 + \left(\frac{R}{R_c}\right)^2},$$

$$V_{\text{ISO}}(R) = V_{\text{inf}} \sqrt{4\phi G \rho_0 (R_c)^2 \left[1 - \left[\frac{R_c}{R} \arctan\left(\frac{R}{R_c}\right) \right] \right]},$$

where ρ_0 is the central core density and R_c is the core radius of the halo. The rotational velocity expression at any radius R , due to an ISO dark matter halo, is V_{ISO} , and the asymptotic velocity of the halo is V_{inf}

- Based on numerical simulations of dark matter halos, Navarro, Frenk & White (Navarro et al. 1996) described the radial density profile with the expressions:

$$\frac{\rho_{\text{NFW}}}{\rho_{\text{crit}}} = \frac{\delta_c}{\frac{R}{R_s} \left(1 + \frac{R}{R_s}\right)^2},$$

$$V_{\text{NFW}}(R) = V_{200} \sqrt{\frac{\ln(1+cx) - \frac{cx}{1+cx}}{x \ln(1+c) - \frac{c}{1+c}}}.$$

where R_s is the characteristic radius of the halo, ρ_{crit} is the critical density of the universe, $c = \frac{R_{200}}{R_s}$ is the concentration parameter and $x = \frac{R}{R_{200}}$. R_{200} is the radius where the average density of the NFW halo is $200\rho_{\text{crit}}$. R_{200} is in kpc and $V_{200} = 0.73R_{200}$ is the rotation velocity at R_{200} in km s⁻¹.

Theoretically, since the FF galaxy is bulge-less, the net rotation velocity V at a radius R is obtained by adding in quadrature the rotational velocity due to the gravitational potential of the stars, gas and DM components:

$$V(R)^2 = \Upsilon_* V_*(R)^2 + V_{\text{gas}}(R)^2 + V_{\text{DM}}(R)^2,$$

where Υ_* is the stellar mass-to-light ratio.

We made use of ROTMAS, a task in GIPSY (van der Hulst et al. 1992b) which allows interactive modelling of rotation curves, with options for the addition of dark matter halo contribution. We carried out the disk-halo decomposition using different assumptions of it: a maximum disk, a minimum disk with gas and a minimum disk.

5. Mass-modelling: Results and discussion

As was already described, the rotation curve fitting procedure typically has as free parameters: the scale-length, the halo density and the mass-to-light ratio of the stellar component. The last value is not known a priori, its estimation is difficult, and may differ from galaxy to galaxy. Cluver et al. (2014) obtained an empirical relationship between mid-infrared emission of galactic disks and stellar mass-to-light ratios in the W1 and W2 WISE bands. Using this relation with the FF WISE photometric measurements available in Wang et al. (2017) we found that $\Upsilon_* = 0.8$.

As the approaching side of the galaxy is clearly kinetically disturbed, we performed the mass-modelling only considering the rotation curve derived from the receding half of the FF galaxy.

5.1. Maximum disk

In the maximum disk model, the stellar disk is scaled to the maximum possible value, dominating the underlying gravitational potential (van Albada et al. 1985). Thus, it returns an upper limit to the Υ_* value and a lower bound on the DM distribution in the galaxy. The *maximum disk* model can be constructed in two different ways; by fixing Υ_* to a maximum possible value, for FF we fixed it at 0.8, or by arbitrary fixing Υ_* at the value which corresponds to the ~75% contribution to the peak of the rotation curve at $R = 2.2r_s$ (Sackett 1997). In Fig. 8 we show the rotation curve decomposition with the *maximum disk* model constructed considering both methods, and in Table 3 we list the results. The values of the mass-to-light ratio Υ_* obtained for the best-fitting models considering the ~75% contribution to the peak of the rotation curve at $R = 2.2r_s$ are an order of magnitude higher than the value derived considering the stellar population. Both ISO and NFW halo give the higher values of reduced χ^2 of all the fits. Previous studies on LSBs and some superthin galaxies indicate that most of these type of galaxies do not have a *maximum disk* (de Blok et al. 2008; Banerjee & Bapat 2017), since the structure in the stellar disk is not seen in the rotation curve.

5.2. Minimum disk

The *minimum disk* model assumes that the rotation curve is entirely due to the presence of dark matter and therefore sets an upper bound on the dark matter density. We constructed two different *minimum disk* models: a *minimum disk with gas*, this model only considers the contribution of the neutral hydrogen and helium to the rotation curve. In Fig. 9, upper panels, we show the rotation curve decomposition with the *minimum disk + gas* and in Table 3 we list the results. And, a *minimum disk* where the stellar and gas disk's contribution are zero. In Fig. 9, lower panels, we show the rotation curve decomposition with the *minimum disk*.

We present the mass-modelling of the FF galaxy, carried out using ISO and NFW DM density profiles; the results are listed in table 3. The best reduced χ^2 values were thrown by the *minimum disk*, especially the one obtained with the NFW DM halo. Thus, the contribution of the visible matter to the net gravitational potential is negligible. This result is in agreement with the trend observed in LSB and other superthin galaxies (de Blok et al. 2008; Banerjee & Bapat 2017; Kurapati et al. 2018). We find that the ratio between the core radius of the halo and the scale-length of the optical disk (R_c/R_D) is always less than two for the ISO DM halo. This indicates that the core of the ISO

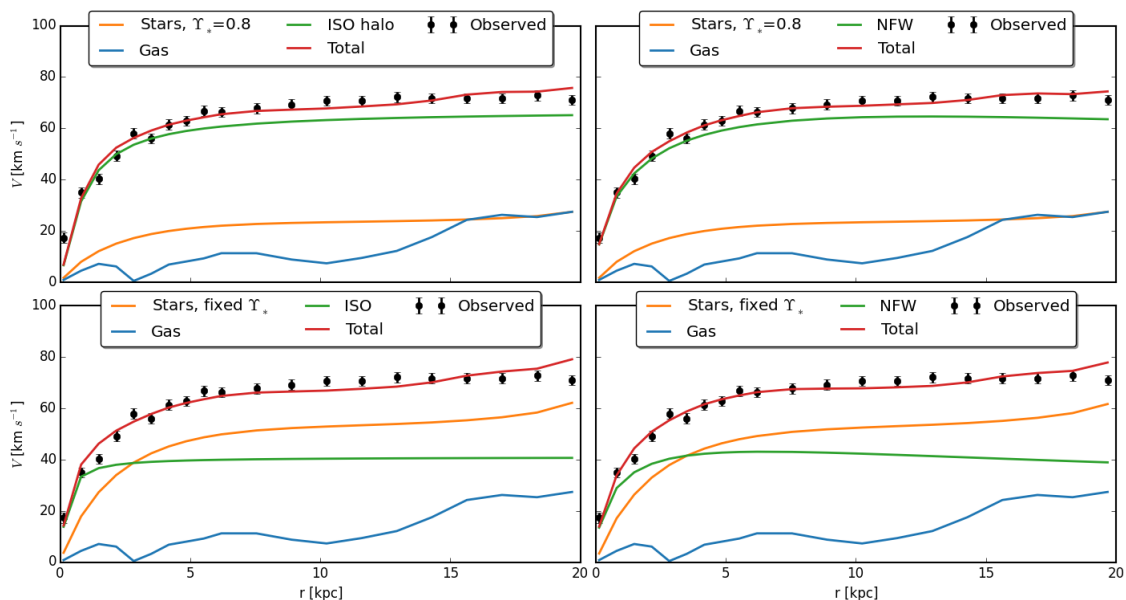


Fig. 8. Modelling H I rotation curve of the Fourcade-Figueroa galaxy. **Upper panels:** ISO and the NFW halo based mass model for the *Maximum disk* with $\Upsilon_{\star}=0.8$. **Lower panels:** ISO and the NFW halo based mass model for the *Maximum disk* considering $\sim 75\%$ contribution to the peak of the rotation curve at $R = 2.2r_{\text{s}}$. The orange line indicates the rotation curve due to the stellar disk, the blue line due to the gas disk, the green line due to the dark matter halo and in red colour the best-fitting model rotation curve.

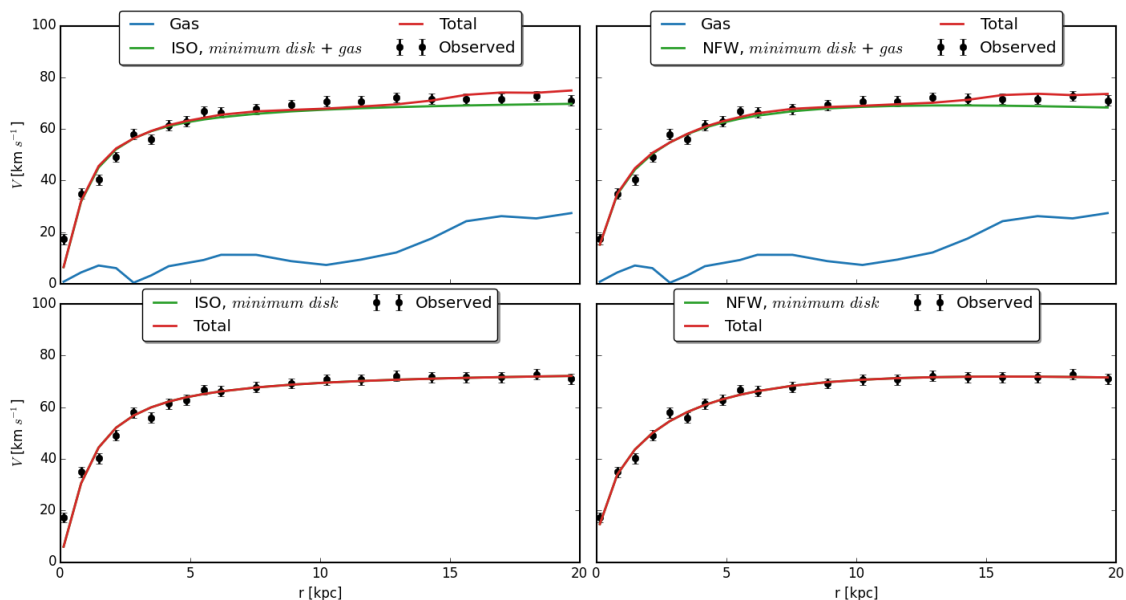


Fig. 9. Modelling H I rotation curve of the Fourcade-Figueroa galaxy. **Upper panels:** ISO and the NFW halo based mass model for the *minimum disk + gas*. **Lower panels:** ISO and the NFW halo based mass model for the FF galaxy for the *minimum disk*. The orange line indicates the rotation curve due to the stellar disk, the blue line due to the gas disk, the green line due to the dark matter halo and in red colour the best-fitting model rotation curve.

halo is compact; consequently, the dark matter halo dominates at the inner radii as well. Banerjee & Bapat (2017) obtained similar results for 3 superthin galaxies (UGC 7321, IC 5249 and IC 2233) as well as Kurapati et al. (2018) (FGC 1540). The compactness of the dark matter halo may be responsible for the superthin disk distribution (Banerjee & Jog 2013).

5.3. Mass-modelling with MOND formalism

The Modified Newtonian Dynamics (MOND) postulates that Newtonian dynamics breaks down at small acceleration (Mil-

grom 1983). This formalism rules out the presence of dark matter and takes into account the self-gravity of the stars and gas in galactic dynamics studies. There are two free parameters: the stellar mass-to-light ratio (Υ_{\star}) and the acceleration per unit length (a_0).

In Fig. 10 we show the best-fitting rotation curve for the MOND formalism. In order to achieve a physically realistic value of a_0 , Υ_{\star} was fixed to 0.8. The acceleration parameter resulted in $a_0 = 2694 \pm 520 \text{ km}^2 \text{ s}^{-1} \text{ kpc}^{-1}$. The reduced χ^2 is 42; this means that in the case of FF the centrally concentrated mass indicated by the RC is not seen in the gas and stellar distribu-

Table 3. Results of the mass modelling of the FF galaxy for ISO and NFW dark matter halo profiles.

Model	Υ_*	Υ_{gas}	R_C	R_C/R_D	ρ_0	χ^2
ISO			[kpc]		[$10^{-3} M_\odot \text{pc}^{-3}$]	
Maximum disk fixed Υ_*	0.8	1.0	0.79 ± 0.11	0.2	131 ± 31	3.2
Maximum disk	4.13	1.0	0.20 ± 0.06	0.05	7165 ± 405	3.0
Minimum disk with gas	0	1.0	0.8 ± 0.1	0.13	126 ± 25	3.2
Minimum disk	0	0	0.9 ± 0.1	0.15	109 ± 18	2.7
Model			c	R_{200}	v_{200}	
NFW				[kpc]	[km s^{-1}]	
Maximum disk fixed Υ_*	0.8	1.0	7.1 ± 0.3	42 ± 1	~ 30	1.0
Maximum disk	4.13	1.0	8.6 ± 1.1	26 ± 1	~ 19	1.8
Minimum disk with gas	0	1.0	7.1 ± 0.3	44.8 ± 0.6	~ 32	0.9
Minimum disk	0	0	6.5 ± 0.2	47.3 ± 0.5	~ 54	0.6

Notes: R_c is the core radius of the ISO DM halo, ρ_0 is the central core density of the ISO DM halo, c is the concentration parameter of the NFW DM halo, R_{200} is the radius where the average density of the NFW DM halo is $200\rho_{\text{crit}}$ and parameters Υ_* and Υ_{gas} are the scaling factor from the stellar and gaseous disk were fixed in order to improve the results.

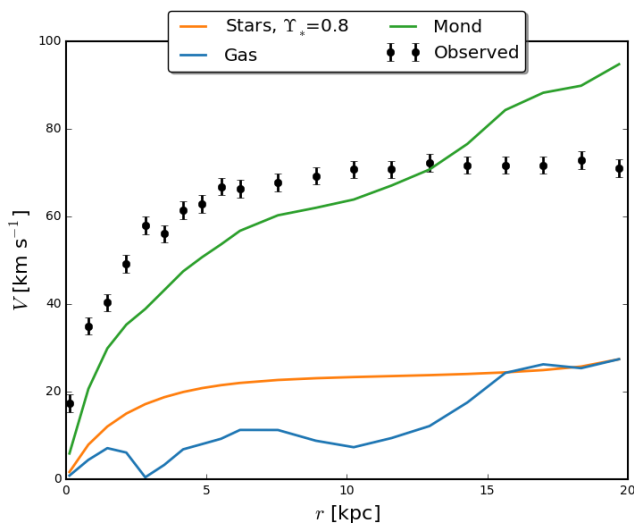


Fig. 10. Modelling H I rotation curve of the Fourcade-Figueroa galaxy using MOND. The orange line indicates the rotation curve due to the stellar disk, the blue line the rotation curve due to the gas disk, and the green line is the MOND best-fitting model rotation curve.

tion. Which means there should be a very concentrated unseen baryonic component for MOND to work.

6. The shred

Despite its superthin structure, the FF galaxy shows an asymmetry towards its north-west-side, clearly observed in both, optical and H I moment maps. A series of features appears in the approaching side of the galaxy: 1) the iso-velocity contours start to exhibit distortions only a few kpc away from the centre; and, at the location of the kinematic anomalies, we can also see a thickening of the emission observed in the integrated moment map. However, due to the edge-on orientation of the galaxy, a more sophisticated analysis is required to determine at which radial location this occurs. And 2) the H I gas steeply flares as the stellar component becomes fainter; this is indicative of the mass in the disk changing (Sancisi & Allen 1979; Olling 1995). Additionally, at the same location, the dispersion velocity is higher.

The de-projected H I peak surface density is $\Sigma_{\text{HI}} \sim 5 M_\odot \text{pc}^{-2}$, close to the mean value proposed by Cayatte et al. (1994) for Sbc galaxies ($\sim 6 M_\odot \text{pc}^{-2}$); this value is also in agreement with the

results found by Kurapati et al. (2018) and Banerjee & Bapat (2017) for similar superthin galaxies. Furthermore, in most of the gas disk of FF, the gas surface density seems to lie below that required for efficient star formation (Kennicutt 1989), and moreover, the overall density profile value is half of the peak surface density, see Fig. 6. Although the galaxy is forming some stars, this result is consistent with the very low star formation rate derived from optical observations ($\log(\text{SFR}) = -1.0 M_\odot \text{yr}^{-1}$) and the low radio continuum emission previously reported (Saponara et al. 2012); The evidence suggests that intense star formation activity is not the main cause of the observed disruption.

In 1992, Thomson (1992), after the analysis of numerical simulations, proposed that the FF shred could be possibly originated because the FF galaxy undergoes a strong prograde interaction with the massive galaxy Cen A. Currently, this theory is ruled out. A recent, more accurate, distance estimates put FF just beyond Cen A (~ 7 Mpc, Karachentsev et al. 2015). Another possible explanation of the observed vertical thickness is the interaction with a companion dwarf galaxy, which enhance star formation in a small region in the western-most part of the disk, generating this and the higher dispersion observed. The available UV images from GALEX³, although they partially cover the galaxy, provide a hint of that. Despite the fact that the FOV is mostly filled with the galaxy, we visually looked for H I low-mass companions of the FF galaxy, but no recognisable companions were observed. However, Cen A seems to have an overabundance of the faintest dwarfs in comparison to its simulated analogues (Müller et al. 2019), indicating that interactions are likely, and the scenario of a dwarf galaxy accreted like the Sag dSph by the Milky Way turns very probable (Ruiz-Lara et al. 2020). This would be contrary to superthins evolving in isolation. Of course, FF could be disturbed in such a way that it is evolving away from being a superthin galaxy although the quiescent and thin approaching side seems to counter this idea. Up to now, most studies on superthin galaxies present this class as isolated objects, that is, devoid of interactions. An exception could be the galaxy IC 2233 for which the authors explore the possibility of interaction with smaller nearby galaxies (Uson & Matthews 2003). That interactions do not destroy the superthin disks in these galaxies fits with previous results (O'Brien et al. 2010; Banerjee & Bapat 2017; Kurapati et al. 2018) indicating

³ <https://archive.stsci.edu/missions-and-data/galex>

that the compact DM halo is the main responsible for the superthin structure of the stellar disk, not isolation.

7. Summary

We use the rotation curve, the H I surface density profile along with the stellar profile obtained from the literature to construct the mass models for the FF galaxy. The FF rotation curve, as well as its de-projected H I surface density profile, were derived by fitting a detailed 3D tilted ring model to the data. After the assumption of the ISO as well as the NFW dark matter halo, we found that both halos fit well the observed rotation curve, but the best reduced χ^2 values were thrown by the *minimum disk* model considering the NFW halo. The results obtained from the mass-modelling implies that the dark matter halo is compact. We derived the thickness of the H I disk as a function of the galactocentric radius and on the approaching side of the galaxy, the vertical H I thickness shows an irregular profile. The FF galaxy shows an asymmetry towards its north-west-side, clearly observed at optical and H I images. The new distance establishes FF away from Cen A, which dismiss the hypothesis of past interaction between them. Even though, we did not find H I low-mass companions for FF in our H I cubes, tidal interaction could not be ruled out. Thus, the compact dark matter halo might be the main responsible for the superthin structure observed in the galaxy and not isolation.

Acknowledgements

JS is grateful to Arunima Banerjee for use full discussions and to Jing Wang for the mass profile. This paper is based on observations obtained with the Australia Telescope Compact Array (ATCA) and the Giant Metrewave Radio Telescope (GMRT). ATCA is part of the Australia Telescope National Facility (ATNF) which is funded by the Australian Government for operation as a National Facility managed by CSIRO. We acknowledge the Gomeroi people as the traditional owners of the Observatory site. GMRT is operated by the National Centre for Radio Astrophysics of the Tata Institute of Fundamental Research. We thank the staff of both radio telescopes who made these observations possible. This research has made use of the NASA/IPAC extragalactic database (NED) that is operated by the Jet Propulsion Laboratory, California Institute of Technology, under contract with the National Aeronautics and Space Administration. This work was partially supported by FCAG-UNLP, and ANPCyT project PICT 2017-0773. PK is partially supported by the BMBF project 05A17PC2 for D-MeerKAT.

References

Banerjee, A. & Bapat, D. 2017, MNRAS, 466, 3753
 Banerjee, A. & Jog, C. J. 2013, MNRAS, 431, 582
 Banerjee, A., Matthews, L. D., & Jog, C. J. 2010, New A, 15, 89
 Begeman, K. G., Broeils, A. H., & Sanders, R. H. 1991, MNRAS, 249, 523
 Cayatte, V., Kotanyi, C., Balkowski, C., & van Gorkom, J. H. 1994, AJ, 107, 1003
 Cluver, M. E., Jarrett, T. H., Hopkins, A. M., et al. 2014, ApJ, 782, 90
 Colomb, F. R., Loiseau, N., & Testori, J. C. 1984, Astrophys. Lett., 24, 139
 Dalcanton, J. J. & Bernstein, R. A. 2000, AJ, 120, 203
 de Blok, W. J. G. & Bosma, A. 2002, A&A, 385, 816
 de Blok, W. J. G., Walter, F., Brinks, E., et al. 2008, AJ, 136, 2648
 de Vaucouleurs, G., de Vaucouleurs, A., Corwin, Jr., H. G., et al. 1991, 1, Vol. 3, Third Reference Catalogue of Bright Galaxies (Berlin Heidelberg New York: Springer-Verlag)
 Fourcade, C. 1970, Bol. Asoc. Argentina de Astron, 16, 10
 Gerritsen, J. P. E. & de Blok, W. J. G. 1999, A&A, 342, 655

Gooch, R. 1996, in Astronomical Society of the Pacific Conference Series, Vol. 101, Astronomical Data Analysis Software and Systems V, ed. G. H. Jacoby & J. Barnes, 80
 Greisen, E. W. 2003, AIPS, the VLA, and the VLBA, Vol. 285 (Astrophysics and Space Science Library), 109
 Ho, L. C., Li, Z.-Y., Barth, A. J., Seigar, M. S., & Peng, C. Y. 2011, ApJS, 197, 21
 Józsa, G. I. G., Kenn, F., Oosterloo, T. A., & Klein, U. 2012, TiRiFiC: Tilted Ring Fitting Code
 Kamphuis, P., Józsa, G. I. G., Oh, S. H., et al. 2015, FAT: Fully Automated TiRiFiC
 Karachentsev, I. D., Karachentseva, V. E., Kudrya, Y. N., Sharina, M. E., & Parnovskij, S. L. 1999, Bulletin of the Special Astrophysics Observatory, 47, 5
 Karachentsev, I. D., Karachentseva, V. E., & Parnovskij, S. L. 1993, Astronomische Nachrichten, 314, 97
 Karachentsev, I. D. & Kudrya, Y. N. 2014, The Astronomical Journal, 148, 50
 Karachentsev, I. D., Tully, R. B., Makarova, L. N., Makarov, D. I., & Rizzi, L. 2015, ApJ, 805, 144
 Kautsch, S. J. 2009, PASP, 121, 1297
 Kennicutt, Robert C., J. 1989, ApJ, 344, 685
 Kennicutt, Robert C., J., Lee, J. C., Funes, J. G., et al. 2008, ApJS, 178, 247
 Koribalski, B. S., Staveley-Smith, L., Kilborn, V. A., et al. 2004, AJ, 128, 16
 Koribalski, B. S., Wang, J., Kamphuis, P., et al. 2018, MNRAS, 467
 Kregel, M., van der Kruit, P. C., & de Grijs, R. 2002, MNRAS, 334, 646
 Kurapati, S., Banerjee, A., Chengalur, J. N., et al. 2018, MNRAS, 479, 5686
 Lauberts, A. & Valentijn, E. A. 1989, The surface photometry catalogue of the ESO-Uppsala galaxies (Astrophysics and Space Science Library)
 Matthews, L. D., Gao, Y., Uson, J. M., & Combes, F. 2005, AJ, 129, 1849
 Matthews, L. D. & Wood, K. 2001, ApJ, 548, 150
 McGaugh, S. S. & de Blok, W. J. G. 1998, ApJ, 499, 41
 Milgrom, M. 1983, ApJ, 270, 365
 Mosenkov, A. V., Sotnikova, N. Y., & Reshetnikov, V. P. 2010, MNRAS, 401, 559
 Müller, O., Rejkuba, M., Pawlowski, M. S., et al. 2019, A&A, 629, A18
 Navarro, J. F., Frenk, C. S., & White, S. D. M. 1996, ApJ, 462, 563
 O'Brien, J. C., Freeman, K. C., & van der Kruit, P. C. 2010, A&A, 515, A63
 Odewahn, S. C. 1994, AJ, 107, 1320
 Olling, R. P. 1995, AJ, 110, 591
 Prasad, J. & Chengalur, J. 2011, FLAGCAL: FLAGging and CALlibration Pipeline for GMRT Data, Astrophysics Source Code Library
 Reshetnikov, V. & Combes, F. 1997, A&A, 324, 80
 Roenback, J. & Bergvall, N. 1995, A&A, 302, 353
 Rubin, V. C., Ford, W. K., J., & Thonnard, N. 1978, ApJ, 225, L107
 Ruiz-Lara, T., Gallart, C., Bernard, E. J., & Cassisi, S. 2020, Nature Astronomy, 4, 965
 Sackett, P. D. 1997, ApJ, 483, 103
 Sancisi, R. & Allen, R. J. 1979, A&A, 74, 73
 Saponara, J., Lefranc, V., Benaglia, P., Andruchow, I., & Koribalski, B. 2012, Boletín de la Asociación Argentina de Astronomía La Plata Argentina, 55, 353
 Sault, R. J., Teuben, P. J., & Wright, M. C. H. 1995, in Astronomical Society of the Pacific Conference Series, Vol. 77, Astronomical Data Analysis Software and Systems IV, ed. R. A. Shaw, H. E. Payne, & J. J. E. Hayes, 433
 Schlegel, D. J., Finkbeiner, D. P., & Davis, M. 1998, ApJ, 500, 525
 Schwarzkopf, U. & Dettmar, R. J. 2001, A&A, 373, 402
 Serra, P., Westmeier, T., Giese, N., et al. 2015, MNRAS, 448, 1922
 Thomson, R. C. 1992, MNRAS, 257, 689
 Toth, G. & Ostriker, J. P. 1992, ApJ, 389, 5
 Tully, R. B., Courtois, H. M., Dolphin, A. E., et al. 2013, AJ, 146, 86
 Uson, J. M. & Matthews, L. D. 2003, AJ, 125, 2455
 van Albada, T. S., Bahcall, J. N., Begeman, K., & Sancisi, R. 1985, ApJ, 295, 305
 van der Hulst, J. M., Terlouw, J. P., Begeman, K. G., Zwitsers, W., & Roelfsema, P. R. 1992a, in Astronomical Society of the Pacific Conference Series, Vol. 25, Astronomical Data Analysis Software and Systems I, ed. D. M. Worrall, C. Biemesderfer, & J. Barnes, 131
 van der Hulst, J. M., Terlouw, J. P., Begeman, K. G., Zwitsers, W., & Roelfsema, P. R. 1992b, in Astronomical Society of the Pacific Conference Series, Vol. 25, Astronomical Data Analysis Software and Systems I, ed. D. M. Worrall, C. Biemesderfer, & J. Barnes, 131
 van der Kruit, P. C. & Searle, L. 1981a, A&A, 95, 105
 van der Kruit, P. C. & Searle, L. 1981b, A&A, 95, 116
 Wang, J., Koribalski, B. S., Jarrett, T. H., et al. 2017, MNRAS, 472, 3029
 Zasov, A. V., Makarov, D. I., & Mikhailova, E. A. 1991, Soviet Astronomy Letters, 17, 374